International Journal of Modern Physics B
2150083 (20 pages)

DOI: 10.1142/S0217979221500831

Optimized frame work for Reiner–Philippoff nanofluid with improved thermal sources and Cattaneo–Christov modifications: A numerical thermal analysis

M. Ijaz Khan[*], Usman[†], Abuzar Ghaffari[‡], Sami Ullah Khan[§], Yu-Ming Chu[¶,‖,††] and Sumaira Qayyum[**]

[*]*Department of Mathematics and Statistics, Riphah International University I-14 Islamabad 44000, Pakistan*

[†]*Beijing Key Laboratory for Magneto-Photoelectrical Composite and Interface Science Department of Applied Mathematics, School of Mathematics and Physics, University of Science and Technology Beijing, Beijing 100083, P. R. China*

[‡]*Department of Mathematics, University of Education, Lahore Attock Campus 43600, Pakistan*

[§]*Department of Mathematics, Comsats University Islamabad, Sahiwal 57000, Pakistan*

[¶]*Department of Mathematics, Huzhou University, Huzhou 313000, P. R. China*

[‖]*Hunan Provincial Key Laboratory of Mathematical Modeling and Analysis in Engineering Changsha University of Science and Technology, Changsha 410114, P. R. China*

[**]*Department of Mathematics, Quaid-I-Azam University 45320, Islamabad 44000, Pakistan*
[††]*chuyuming@zjhu.edu.cn*

AQ: Please check and approve author's affiliations.

Received 28 September 2020
Revised 29 December 2020
Accepted 30 December 2020
Published

This motivating analysis aims to present the thermal mechanism for mixed convection flow of Reiner–Philippoff nanofluid with assessment of entropy generation. The thermal performances of nanomaterials have been modified by utilizing the nonuniform heat source/sink, Ohmic dissipations and thermal radiation consequences. The assumed surface is assumed to be porous with non-Darcian porous medium. The modified Cattaneo–Christov relations are followed to modify the mass and heat equations. The invoking of similarity variables results in differential equations in nonlinear and coupled form. A MATALB-based shooting algorithm is employed to access the numerical simulations.

[††]Corresponding author.

AQ: Please check.

The physical aspect of thermal model is graphically addressed for endorsed flow parameters. The importance of entropy generation is visualized with associated mathematical relations and physical explanations. The numerical values are obtained for the assessment of heat and mass transfer phenomenon.

Keywords: Reiner–Philippoff nanofluid; entropy generation; nonuniform heat source/sink; Cattaneo–Christov law; numerical scheme.

AQ: Please provide PACS numbers.

1. Introduction

Nanofluids are made up of mixture of base fluids like water, ethylene glycol, engine oil, etc. and nanoparticles to enhance the thermal properties of these base fluids. Actually, base fluids are usually with less thermal conductivity such as water has thermal conductivity of only 0.613 W/mk where the thermal conductivity of nanoparticle Ag (silver) is 429 W/mk. So, when we mix these two thermal conductivities, the fluid enhances drastically which is the main purpose of nanofluid. Nanoparticles are of size (1–100 nm) diameter and nanoparticles in base fluids are used in minimum possible concentrations. As a rough estimate, by adding nanoparticles into base fluids base fluid thermal, conductivity enhances in the range of 15–40%. Nanofluids have several useful applications such as cancer therapy, nuclear reactor cooling, transformer cooling and vehicle computers. Choi[1] was the one who worked on enhancement of thermal conductivity for base fluid by adding nanoparticles. Elbashbeshy *et al.*[2] used the nanofluids during the process of cooling in the heat treatment of metals. Bachok *et al.*[3] elucidated the effect of stagnation point nanofluid flow due to shrinking/stretching sheet. MHD flow of nanofluid in presence of viscous dissipation and chemical reaction is studied by Kameswaran *et al.*[4] Laminar flow of nanofluid is incorporated by Narayana *et al.*[5] In this study, it is showed that as the nanoparticles volume fraction increases, axial and free stream velocity decays. Basic concept about thermophysical properties of nanofluid such as viscosity, thermal diffusivity and thermal conductivity is provided by Kang *et al.*[6] and Rudyak *et al.*[7] Exact solution of nanofluid flow with suction/injection is developed by Elbashbeshy *et al.*[8] Jafar *et al.*[9] worked on effects of Joule heating, MHD and viscous dissipation over a stretching/shrinking sheet. Flow of viscous fluid by deformation of a surface is studied by Pavlov.[10]

Heat transfer between the two objects is essential when there is difference in their temperatures. Fourier gave the concept of heat transfer but there are some defects in his model, so several researchers modified his law. Main flaw in his model is that heat transfer is very spontaneous. For example, if we gave heat to the end of the rod, it will be felt at the other end of the rod at the same time which is not possible because heat takes time to transfer. So, keeping in mind this limitation, Cattaneo[11] added the relaxation time in Fourier's law. Relaxation time is a time taken by a medium to transfer the heat to its neighboring particles. After this, Christov[12] also expressed Cattaneo's formula with the help of Oldroyd's upper-convective differentiation. This model is now known as Cattaneo–Christov (C-C) heat flux model. Straughan[13] used this model for viscous fluid flow. Maxwell fluid

AQ: Please check running head title.

motion with non-Fourier heat flux model is examined by Han *et al.*[14] 3D flow of mass diffusivity and heat conduction is elucidated by Hayat *et al.*[15] Some various studies about non-Fourier heat flux model can be seen through Refs. 16–22.

There are several models of non-Newtonian fluids which are proposed for different hydrodynamic and hydromagnetic behaviors. One of the most important non-Newtonian fluid models is named as "Reiner–Philippoff fluid". There is a very less literature in this work of field. 2D flow of R-P fluid is examined by Kapur and Gupta.[23] Reiner–Philippoff fluid flow over a circular tube is elucidated by Ghoshal.[24] Na[25] and Yam *et al.*[26] explained the boundary layer flow of R-P fluids over a wedge. References 27–35 are highlighted the recent development in the field of stretched flow versus various flow geometries.

AQ: Please check sentence for clarity.

Main purpose of this paper is to examine the motion of R-P fluid with Darcy Forchheimer fluid. Irreversibility factor is analyzed in presence of thermal radiation, Porous medium, heat and mass transfer. Non-Fourier heat and mass fluxes are used to analyze the heat and mass transfer. For this purpose, Cattaneo–Christov double diffusion model is used. Velocity slip effect is incorporated in boundary condition for momentum equation. Thermal dependent heat source sink and activation energy effect is analyzed in heat and mass transfer effect. A MATLAB-based shooting algorithm is utilized to find the convergent solutions. Trends of velocity, temperature, entropy generation, Bejan number, concentration profile, skin friction, Sherwood number and Nusselt number are shown through graphs.

2. Mathematical Formulation

Consider a steady two-dimensional (2D) bioconvection flow of viscous incompressible R-P nanofluid upon a nonlinearly stretching sheet. The sheet is embedded in a saturated non-Darcian porous medium with viscous and Ohmic dissipations. The cartesian coordinate is selected so that x-axis is chosen along with the sheet, whereas y-axis is normal to it. The Cattaneo–Christov heat flux model is used to study heat and mass transfer characteristics. The features of nanofluid are analyzed and validated for Thermophoresis and Brownian motion through the Buongiorno mathematical model. The effects of temperature-dependent heat source/sink and activation energy are incorporated in heat and concentration equations. The fluid is maintained at the surface through the temperature T_f and concentration C_f. The fluid which is flowing away from the boundary layer is prescribed at a uniform temperature T_∞ and concentration C_∞ with $T_f > T_\infty$ and $C_f > C_\infty$.

The relationship between shear-stress τ and shear-strain $\frac{\partial u}{\partial y}$ for the R-P fluid model is delineated as follows:

$$\frac{\partial u}{\partial y} = \frac{\tau}{\mu_\infty + \frac{\mu_0 - \mu_\infty}{1+\frac{\tau}{\tau_s}}}, \tag{1}$$

where τ_s is the reference shear-stress. The quantities like μ_0 and μ_∞, respectively, denote the corresponding zero-shear and upper Newtonian limiting viscosities. The

R-P fluid model predicts the Newtonian behavior for small and large shear stresses, whereas, for intermediate values of shear stresses, it shows the non-Newtonian behavior.

Thus, in the light of the above-stated assumptions, the governing equations can be written as follows[23,25,26]:

$$\frac{\partial u}{\partial x} + \frac{\partial v}{\partial y} = 0, \tag{2}$$

$$\begin{aligned} u\frac{\partial u}{\partial x} + v\frac{\partial v}{\partial y} &= \frac{1}{\rho_f}\frac{\partial \tau}{\partial y} - \frac{\upsilon_f}{\rho_f K^*} - \frac{F}{\sqrt{K^*}}u^2 \\ &\quad + \frac{1}{\rho_f}[\rho_{f\infty}\beta^* g^*(1-C_\infty)(T-T_\infty) - (\rho_p - \rho_{f\infty})g^*(C-C_\infty)], \end{aligned} \tag{3}$$

$$\begin{aligned} u\frac{\partial T}{\partial x} + v\frac{\partial T}{\partial y} &= \alpha_f^*\frac{\partial^2 T}{\partial y^2} - \frac{1}{(\rho c_p)_f}\frac{\partial q}{\partial y} + \frac{\mu_f}{(\rho c_p)_f}\left(\frac{\partial u}{\partial y}\right)^2 \\ &\quad - \Gamma_T\left[u\frac{\partial u}{\partial x}\frac{\partial T}{\partial x} + v\frac{\partial v}{\partial y}\frac{\partial T}{\partial y} + u\frac{\partial v}{\partial x}\frac{\partial T}{\partial y} + v\frac{\partial u}{\partial y}\frac{\partial T}{\partial x} + 2uv\frac{\partial^2 T}{\partial x\partial y}\right. \\ &\quad \left. + u^2\frac{\partial^2 T}{\partial x^2} + v^2\frac{\partial^2 T}{\partial y^2}\right] + \tau^*\left[D_B\frac{\partial T}{\partial y}\frac{\partial C}{\partial y} + \frac{D_T}{T_\infty}\left(\frac{\partial T}{\partial y}\right)^2\right] + \frac{q'''}{(\rho c_p)_f}, \end{aligned} \tag{4}$$

$$\begin{aligned} u\frac{\partial C}{\partial x} + v\frac{\partial C}{\partial y} &= D_B\frac{\partial^2 C}{\partial y^2} + \frac{D_T}{T_\infty}\frac{\partial^2 T}{\partial y^2} - k_r^2(C-C_\infty)\exp\left(\frac{-E_a}{\kappa T}\right) \\ &\quad - \Gamma_C\left[u\frac{\partial u}{\partial x}\frac{\partial C}{\partial x} + v\frac{\partial v}{\partial y}\frac{\partial C}{\partial y} + u\frac{\partial v}{\partial x}\frac{\partial C}{\partial y} + v\frac{\partial u}{\partial y}\frac{\partial C}{\partial x} + 2uv\frac{\partial^2 C}{\partial x\partial y}\right. \\ &\quad \left. + u^2\frac{\partial^2 C}{\partial x^2} + v^2\frac{\partial^2 C}{\partial y^2}\right], \end{aligned} \tag{5}$$

where u, v are the velocity components along x, y. The quantities like $\rho_f, \upsilon_f, F, K^*, \rho_p, \beta^*$ and g^* denote the nanofluid density, kinematic viscosity, drag coefficient, the permeability of the porous medium, nanoparticles density, thermal expansion coefficient and gravitational acceleration, T is the temperature, $\alpha_f^*, (\rho c_p)_f, \mu_f$ are the thermal diffusivity, heat capacity at constant pressure, dynamic viscosity, $\Gamma_T, \tau^*, D_B, D_T$ represent the relaxation time of heat flux, heat capacity ratio, Brownian diffusion coefficient, thermophoresis coefficient, C is the nanoparticles concentration, k_r, E_a, κ and Γ_C signify the chemical reaction constant rate, activation energy, Boltzmann constant and relaxation time of mass flux.

The linearized form of radiative heat flux q in terms of Rosseland approximation is given by

$$q = \frac{-4\sigma^*}{3k^*}\frac{\partial T^4}{\partial y}. \tag{6}$$

Here, σ^* and k^* refer to the Stefan–Boltzmann constant and mean absorption coefficient, respectively.

The temperature-dependent nonuniform heat source/sink q''' is defined as follows:

$$q''' = \frac{k_\infty U_w(x)}{x\upsilon_f}[A^*(T_f - T_\infty)e^{-\eta} + B^*(T - T_\infty)], \tag{7}$$

where A^* and B^* are the heat generation and absorption parameters.

The appropriate boundary conditions are

$$u = U_w(x) = ax^{1/3}, \quad v = 0, \quad T = T_f, \quad C = C_f, \quad \text{at } y = 0, \tag{8}$$

$$u \to 0, \quad T \to T_\infty, \quad C \to C_\infty \text{ at } y = \infty, \tag{9}$$

2.1. *Similarity transformation*

The similarity transformation for the present problem is chosen as

$$\begin{gathered} \eta = \sqrt{\frac{a}{\upsilon_f}}\frac{y}{x^{1/3}}, \quad \psi = \sqrt{a\upsilon_f}x^{2/3}f(\eta), \quad \tau = \sqrt{a^3\upsilon_f}g(\eta), \\ \theta(\eta) = \frac{T - T_\infty}{T_f - T_\infty}, \quad \varphi(\eta) = \frac{C - C_\infty}{C_f - C_\infty}. \end{gathered} \tag{10}$$

Upon inserting (10) into (1–5), we get the following dimensionless system of equations:

$$g = f''\frac{g^2 + \lambda\gamma^2}{g^2 + \gamma^2}, \tag{11}$$

$$g' = \frac{1}{3}f'^2 - \frac{2}{3}ff'' - K_p f' - F_r f'^2 + \alpha(\theta - \mathrm{Nr}\varphi), \tag{12}$$

$$\begin{aligned} &(1 + \mathrm{Rd})\theta'' + \frac{2}{3}\Pr f\theta' + \Pr \mathrm{Ec} f'^2 + \Pr N_b\theta'\varphi' + \Pr N_t\theta'^2 \\ &\qquad - \Pr \lambda_T(ff'\theta' + f^2\theta'') + A^*e^{-\eta} + B^*\theta = 0, \end{aligned} \tag{13}$$

$$\begin{aligned} &\varphi'' + \mathrm{Le}\Pr f\varphi' + \frac{N_t}{N_b}\theta'' - \lambda_C(ff'\varphi' + f^2\varphi'') \\ &\qquad - \Pr \mathrm{Le}\sigma\varphi(1 + \delta\theta)^n \exp\left(\frac{-E_1}{1 + \delta\theta}\right) = 0. \end{aligned} \tag{14}$$

The transformed boundary conditions are

$$f(\eta) = 0, \quad f'(\eta) = 1, \quad \theta(\eta) = 1, \quad \varphi(\eta) = 1, \quad \text{at } \eta = 0, \tag{15}$$

$$f'(\eta) \to 0, \quad \theta(\eta) \to 0, \quad \varphi(\eta) \to 0, \quad \text{at } \eta \to \infty. \tag{16}$$

The parameters which help the fluid to govern are listed as follows:

$$\lambda = \frac{\mu_0}{\mu_\infty}, \quad \gamma = \frac{\tau_s}{\sqrt{a^3\upsilon_f}}, \quad K_p = \frac{\upsilon_f x^{2/3}}{k^* a}, \quad F_r = \frac{F}{\sqrt{K^*}},$$

$$\alpha = \frac{\beta^* g^*(1 - C_f)(T_f - T_\infty)}{aU_w}, \quad \lambda_T = \frac{\Gamma_T a}{x^{2/3}},$$

$$\mathrm{Nr} = \frac{(\rho_p - \rho_{f\infty})(C_f - C_\infty)}{\rho_f \beta(1 - C_\infty)(T_f - T_\infty)}, \quad \lambda_C = \frac{\Gamma_C a}{x^{2/3}}, \quad E_1 = \frac{E_a}{\kappa T_\infty},$$

$$\sigma = \frac{k_r^2 x^{2/3}}{a}, \quad \delta = \frac{T_f - T_\infty}{T_\infty}, \quad \mathrm{Le} = \frac{\upsilon_f}{D_B},$$

$$N_t = \frac{\tau^* D_T(T_f - T_\infty)}{\upsilon_f T_\infty}, \quad N_b = \frac{\tau^* D_B(C_f - C_\infty)}{\upsilon_f}, \quad \mathrm{Pr} = \frac{\upsilon_f}{\alpha_f^*},$$

$$\mathrm{Rd} = \frac{16\sigma^* T_f^3}{3k_f k^*}, \quad \mathrm{Ec} = \frac{(ax^{1/3})^2}{(T_f - T_\infty)}, \tag{17}$$

where λ is the R-P fluid parameter, γ is the Bingham number, K_p is the Permeability parameter of the porous medium, F_r is the Forchheimer number, α is the Mixed convection parameter, Nr is the Buoyancy ratio parameter, λ_T is the Thermal relaxation parameter of heat flux, λ_C is the Concentration relaxation parameter of mass flux, E_1 is the Activation parameter, σ is the Chemical reaction parameter, δ is the temperature difference parameter, Le is the Lewis number, N_t and N_b are the thermophoresis and brownian motion parameters, Pr is the Prandtl number, Rd is the radiation parameter and Ec is the Eckert parameter.

2.2. *Nusselt number and Sherwood number*

The following relation defines the local Nusselt number:

$$\mathrm{Nu}_x = \frac{xq_w}{k_f(T_f - T_\infty)}, \quad q_w = k_f \frac{\partial T}{\partial y} - \frac{16\sigma^*}{3k_f k^*} \frac{\partial T}{\partial y}. \tag{18}$$

The non-dimensional form will lead to

$$\frac{\mathrm{Nu}_x}{\sqrt{\mathrm{Re}}} = -(1 + \mathrm{Rd})\theta'(0). \tag{19}$$

Similarly, the non-dimensional form of the local Sherwood number is as follows:

$$\frac{\mathrm{Sh}_x}{\sqrt{\mathrm{Re}}} = -\varphi'(0). \tag{20}$$

3. Entropy Generation and Bejan Number

The mathematical form of Entropy generation can be expressed as

$$S_G = \frac{k_f}{T_\infty^2}\left(1 + \frac{16\sigma^* T_\infty^3}{3k_f k^*}\right)\left(\frac{\partial T}{\partial y}\right)^2 + \frac{\mu_f}{T_\infty}\left(\frac{\partial u}{\partial y}\right)^2 + \frac{\mu_f}{T_\infty K^*}u^2 + \frac{\mathrm{RD}_B}{T_\infty}\left(\frac{\partial T}{\partial y}\right)\left(\frac{\partial C}{\partial y}\right) + \frac{RD_B}{C_\infty}\left(\frac{\partial C}{\partial y}\right)^2, \tag{21}$$

The dimensionless form can be obtained upon utilizing (11) into (21) as follows:

$$N_G = \delta(1 + \mathrm{Rd})\theta'^2 + \mathrm{Br}f''^2 + \mathrm{Br}K_p f'^2 + L\theta'\varphi' + L\frac{\alpha_2}{\delta}\varphi'^2, \tag{22}$$

where

$$N_G = \frac{S_G T_\infty \upsilon_f x^{2/3}}{(T_f - T_\infty) a k_f}, \quad \mathrm{Br} = \frac{\mu_f (a x^{1/3})^2}{k_f \Delta T},$$
$$L = \frac{\mathrm{RD}_B (C_f - C_\infty)}{C_\infty}, \quad \alpha_2 = \frac{(C_f - C_\infty)}{C_\infty}, \tag{23}$$

where N_G, Br, L and α_2 imply the total entropy generation parameter, Brinkman number, Diffusion parameter and concentration difference parameter.

The Bejan number Be is expressed as the ratio of entropy generation because of heat and mass transferred to that of total entropy generation, i.e.,

$$\mathrm{Be} = \frac{\delta(1+\mathrm{Rd})\theta'^2 + L\theta'\varphi' + L\frac{\alpha_2}{\delta}\varphi'^2}{\delta(1+\mathrm{Rd})\theta'^2 + \mathrm{Br} f''^2 + \mathrm{Br} K_p f'^2 + L\theta'\varphi' + L\frac{\alpha_2}{\delta}\varphi'^2}. \tag{24}$$

4. Shooting Method

The shooting method is employed to deal with the nonlinear system of Eqs. (11)–(14) with boundary conditions (15)–(16) because of its low computational cost and higher accuracy. In the shooting method, the boundary value problem (BVP) is required to transform into the initial value problem (IVP) through the following assumptions:

$$f = y_1, \quad f' = y_2, \quad g = y_3, \quad \theta = y_4, \quad \theta' = y_5, \quad \varphi = y_6, \quad \varphi' = y_7. \tag{25}$$

Inserting (25) into the BVP (11)–(14), the following IVP can be obtained:

$$\begin{aligned}
y_1' &= y_2, \\
y_2' &= \frac{y_3(y_3^2 + \gamma^2)}{y_3^2 + \lambda\gamma^2}, \\
y_3' &= \frac{1}{3} y_2^2 - y_1 \left(\frac{y_3(y_3^2+\gamma^2)}{y_3^2 + \lambda\gamma^2} \right) - K_p y_2 - F_r y_2^2 + \alpha(y_4 - \mathrm{Nr} y_6), \\
y_4' &= y_5, \\
y_5' &= -\frac{\begin{array}{c}\frac{2}{3}\Pr y_1 y_5 + \Pr \mathrm{Ec} y_2^2 + \Pr N_b y_5 y_7 + \Pr N_t y_5^2 \\ -\lambda_T(y_1 y_2 y_5) + A^* e^{-\eta} + B^* y_4\end{array}}{1 + \mathrm{Rd} - \lambda_T y_1^2}, \\
y_6' &= y_7, \\
y_7' &= -\frac{\mathrm{Le}\Pr y_1 y_7 + \frac{N_t}{N_b} y_5' - \lambda_C(y_1 y_2 y_7) - \Pr \mathrm{Le}\sigma y_6 (1+\delta y_4)^n \exp\left(\frac{-E_1}{1+\delta y_4}\right)}{1 - \lambda_C y_1^2},
\end{aligned} \tag{26}$$

The boundary conditions become

$$\begin{aligned}
&y_1(\eta) = 0, \quad y_2(\eta) = 1, \quad y_3(\eta) = a_1, \quad y_4(\eta) = 1, \quad y_5(\eta) = a_2, \\
&y_6(\eta) = 1, \quad y_7(\eta) = a_3, \quad \text{at } \eta = 0,
\end{aligned} \tag{27}$$

$$y_2(\eta) \to 0, \quad y_4(\eta) \to 0, \quad y_6(\eta) \to 0, \quad \text{at } \eta \to \infty, \tag{28}$$

where a_1, a_2 and a_3 be the missing initial conditions. First, the value of η_∞ can be chosen arbitrarily. Second, the initial guesses are adjusted as $a_1 = a_2 = a_3 = 1$. Third, the RK-Method of order fourth-fifth is used to solve the ODEs. Fourth, Newton's method is used to specify the accuracy of the calculated values of missing initial.

5. Physical Analysis of Results

The effects of the several types of governing parameters upon the non-dimensional distributions of the velocity $f'(\eta)$, temperature $\theta(\eta)$, concentration $\varphi(\eta)$, entropy generation N_G and Bejan number Be are analyzed graphically.

5.1. *Velocity profiles*

Figures 1–3 are depicted to examine the upshots of the R-P fluid parameter, Bingham number γ, permeability parameter of the porous medium K_p, Forchheimer number F_r, buoyancy ratio parameter Nr and mixed convection parameter α upon the non-dimensional distribution of the velocity $f'(\eta)$.

The effects of the parameters λ and γ upon $f'(\eta)$ are captured in Fig. 1. It is observed that $f'(\eta)$ is observed using two different trends along η for rising values of the parameters λ and γ. The velocity profile $f'(\eta)$ increases as R-P fluid parameter λ increases. The parameter λ describes the ratio of zero rate shear viscosity to that of upper Newtonian limiting viscosity. Therefore, rise in the parameter λ leads to a decrease in the viscosity, which helps the fluid move more freely. The parameter γ shows the ratio of reference shear-stress to the viscous stress. Therefore, the rise in the parameter γ implies the increase in the shear rate, and as a result, the apparent viscosity increases, which decrease the fluid velocity. Also, the boundary layer thickness is thicker for.

The impacts of the parameters F_r and K_p upon $f'(\eta)$ are exhibited in Fig. 2. The profile $f'(\eta)$ is decreasing for higher estimations of both the parameters (F_r, K_p).

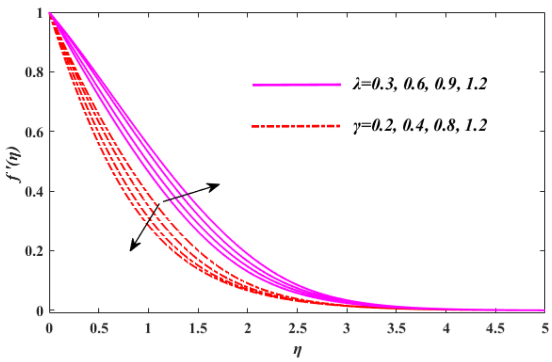

Fig. 1. (Color online) Effects of γ and λ upon $f'(\eta)$.

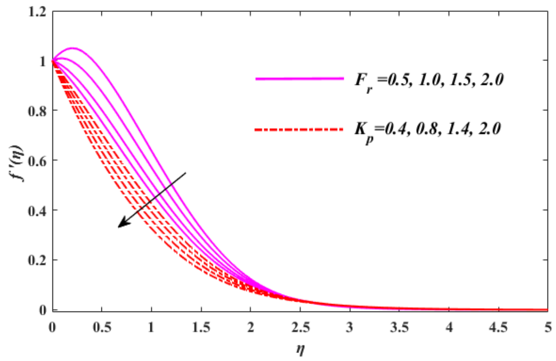

Fig. 2. (Color online) Effects of F_r and K_p upon $f'(\eta)$.

Forchheimer number F_r is in direct relationship with the porosity of medium and drag coefficient. Therefore, the rise in the parameter F_r causes the enhancement in the porosity of medium and drag coefficient, and as a result, the resistive force enhances because of which the fluid velocity decreases. Further, the increase in the Permeability parameter of the porous medium K_p regime becomes more porous because of which resistance towards the fluid motion is increased, and as a result, fluid velocity decreases.

The impressions of the parameters α and Nr upon $f'(\eta)$ are presented in Fig. 3. It is noticed that the velocity profile $f'(\eta)$ is enhanced for the mixed convection parameter α, whereas it reduces for Buoyancy ratio parameter Nr. The mixed convection parameter is the ratio of buoyancy to inertial forces. It is noted that $\alpha = 0$ and $\alpha \neq 0$ correspond to the absence and presence of the mixed convection parameter, respectively. It is further noted that $\alpha > 0$ implies the heat convection from the surface of the sheet towards the flow, i.e., cooling of the sheet surface or heating the fluid. Thus, rise in the mixed convection parameter causes α the enhancement of the buoyancy forces because of which fluid velocity enhances. Also, with the

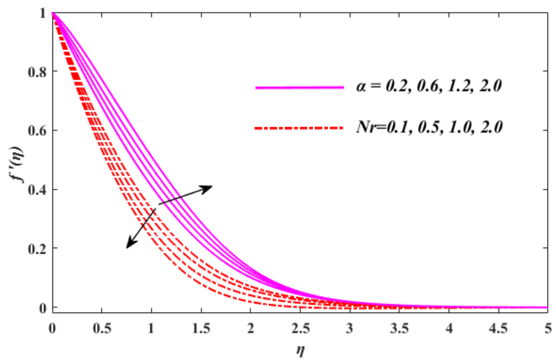

Fig. 3. (Color online) Effects of α and Nr upon $f'(\eta)$.

enhancement of the Buoyancy ratio parameter Nr, the negate buoyancy is increased, which affects the fluid motion and as a result, fluid velocity decays.

5.2. *Temperature profile*

The effects of the parameters like Eckert number Ec, radiation parameter Rd, thermophoresis parameter N_t, Brownian motion parameter N_b, thermal relaxation parameter of heat flux λ_T, Prandtl number Pr and heat source/sink parameters A^*, B^*.

Figure 4 shows the effects of the parameters Ec and Rd upon $\theta(\eta)$. The dimensionless distribution of the temperature $\theta(\eta)$ is witnessed escalating along η for rising values of the Eckert number Ec and radiation parameter Rd. The Eckert number demonstrates the impact of the viscous dissipation. The higher estimations of the Eckert number Ec cause the conversion of the kinetic energy into heat energy, which improves the thermal conductivity of the fluid, and as a result, fluid temperature escalates. Also, augmentation in the radiation parameter Rd leads to the diminution in the mean absorption coefficient because of which more heat is delivered in the fluid direction due to which fluid temperature enhances.

Figure 5 demonstrates the upshots of the parameters N_t and N_b upon $\theta(\eta)$ along η. The non-dimensional distribution of the temperature $\theta(\eta)$ augments for higher estimations of the thermophoresis and Brownian motion parameters (N_t, N_b). The arbitrary motion of the fluid particles escalates with a stronger Brownian motion effect under the action of a strong thermophoretic force produced by the stronger thermophoresis factor. The boundary layer thickness increases as both the parameter increase and this increase is more noticeable for the thermophoresis parameter.

The effects of the parameters λ_T and Pr upon $\theta(\eta)$ along η are provided in Fig. 6. It is noticed that the dimensionless distribution of the temperature $\theta(\eta)$ decays for larger values of the thermal relaxation parameter of heat flux λ_T, Prandtl number Pr. The Cattaneo–Christov heat flux model transformed into classical Fourier's law when $\lambda_T = 0$ and heat energy is instantaneously transferred into R-P fluid.

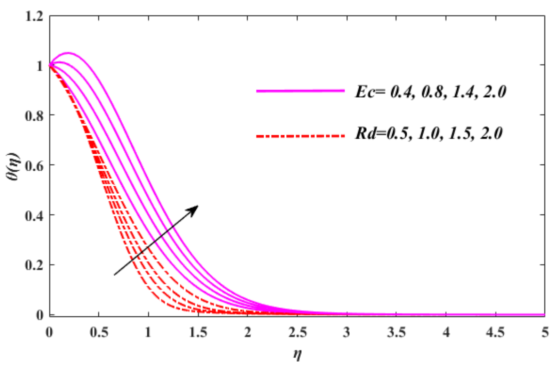

Fig. 4. (Color online) Effects of Ec and Rd upon $\theta(\eta)$.

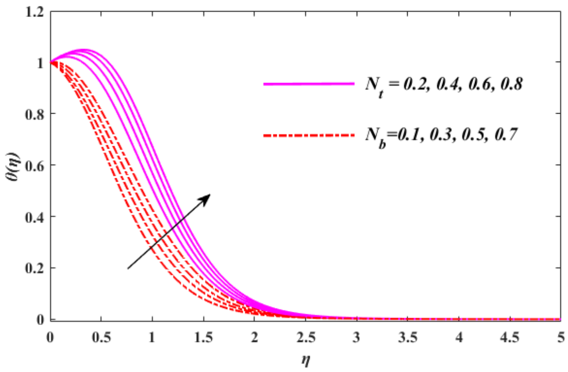

Fig. 5. (Color online) Effects of N_t and N_b upon $\theta\eta$.

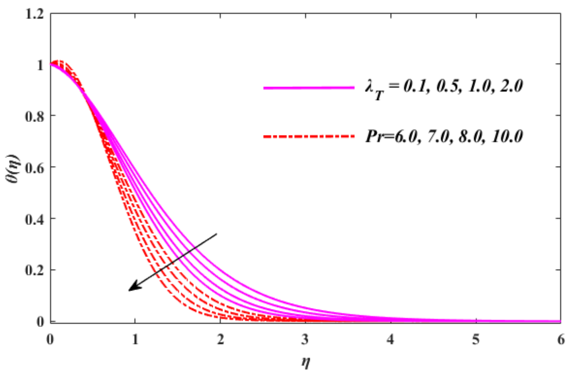

Fig. 6. (Color online) Effects of λ_T and Pr upon $\theta\eta$.

Whereas for nonzero λ_T the Cattaneo–Christov model effectively controls the fluid temperature. Also, the temperature $\theta(\eta)$ decreases as the Prandtl number increases Pr. Because the Prandtl number Pr is associated with thermal and momentum diffusivities, and rise in the Prandtl number causes the dominance of momentum diffusivity over thermal diffusivity because of which temperature decreases within the boundary layer.

Figure 7 encapsulates the impacts of A^* and B^* along η upon $\theta(\eta)$. The parameters A^* and B^* are the space and temperature-dependent parameters of heat source/sink. The positivity of these parameters corresponds to the heat generation, and the negativity of these parameters implies heat absorption. A substantial amount of heat is generated during the process of internal heat source, and as a result, temperature enhances, whereas a large amount of energy is absorbed during the process of internal heat sink due to which temperature decays. With the enhancement of both the parameters, the boundary layer thickness enhances and this enhancement is more extensive for A^*.

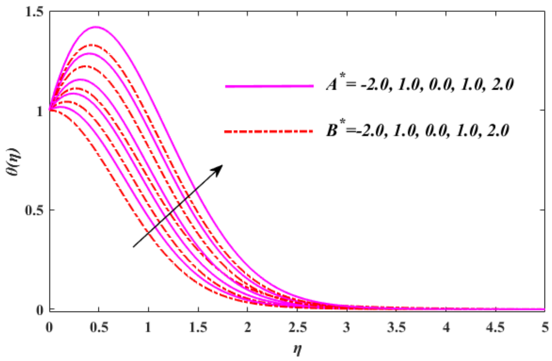

Fig. 7. (Color online) Effects of A^* and B^* upon $\theta\eta$.

5.3. *Concentration profile*

Figures 8–10 demonstrate the effects of the thermophoresis parameter N_t, Brownian motion parameter N_b, Lewis number Le, concentration relaxation parameter of mass flux λ_C, activation energy parameter E_1 and Prandtl number Pr upon the non-dimensional profile of the concentration of nanoparticles $\varphi(\eta)$.

The influences of the parameters N_t and N_b upon $\varphi(\eta)$ are portrayed in Fig. 8. The concentration profile observes two opposite trends for Thermophoresis and Brownian motion parameters (N_t, N_b). The concentration enhances for rising values of the Thermophoresis parameter N_t. The number of nanoparticles increases as the Thermophoresis parameter N_t increases due to which they move from hot to the cold surface and as a result concentration of nanoparticles enhances. In the case of Brownian motion, an unsystematic movement between the nanoparticles occurs. Therefore, the rise in the Brownian motion parameter causes the increment in this unsystematic movement because of which the nanoparticles concentration enhances.

Figure 9 is drawn to elucidate the effects of the parameters λ_C and Le along η upon $\varphi(\eta)$. It witnesses from the figure that the concentration profile is decaying for

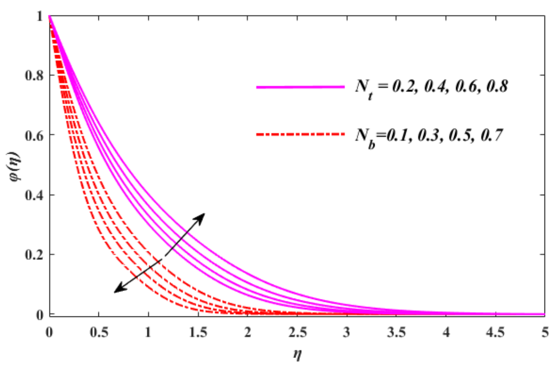

Fig. 8. (Color online) Effects of N_t and N_b upon $\varphi(\eta)$.

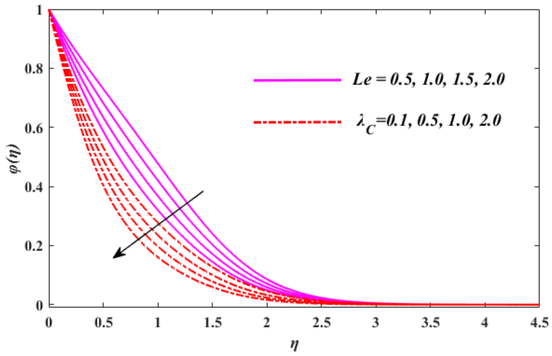

Fig. 9. (Color online) Effects of Le and λ_C upon $\varphi(\eta)$.

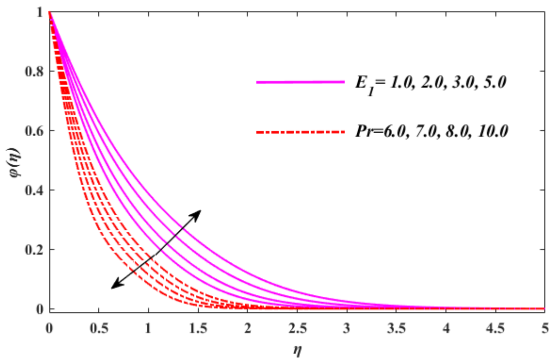

Fig. 10. (Color online) Effects of E_1 and Pr upon $\varphi(\eta)$.

higher estimations of the Lewis number Le and concentration relaxation parameter of mass flux λ_C. The Lewis number Le and Brownian diffusion coefficient D_B are inversely proportional to each other. Therefore, enhancement in the Lewis number Le implies the weaker D_B because of which particles diffuse deeply in the fluid, and as a result, nanoparticles concentration reduces. Further, the rise in the parameter λ_C means that the nanoparticles need more time to diffuse, which causes a decrease in the concentration profile $\varphi(\eta)$.

The effects of the parameters E_1 and Pr upon $\varphi(\eta)$ along η are explained in Fig. 10. The profile of nanoparticles concentration predicts two diverse trends for growing values of both the parameters (E_1, Pr). The profile $\varphi(\eta)$ increases as the Arrhenius activation parameter E_1 increases. Because of the higher estimation of E_1 a gradual decrease in the chemical reaction rate is noticed, and as a result, the concentration enhances. It is also seen that the concentration profile $\varphi(\eta)$ decays as Prandtl number enhances. The increase in the Prandtl number implies the weaker D_B which may enhance the temperature, but it reduces the nanoparticles concentration. Also, the thickness of the concentration boundary layer is thicker for the parameters E_1 whereas it is thinner for the parameter Pr.

6. Entropy Generation and Bejan Number Analysis

The effects of the temperature difference parameter δ, concentration difference parameter α_2, radiation parameter Rd, Brinkman number Br, diffusion parameter L and the permeability parameter of the porous medium K_p upon the non-dimensional distributions of Entropy generation N_G and Bejan number Be are depicted in Figs. 11–16. The impacts of the parameters δ and α_2 upon N_G and Be are presented in Figs. 11 and 12. It is noticed that the non-dimensional profiles of entropy generation N_G and Bejan number Be are increasing functions along η of the temperature difference parameter δ, concentration difference parameter α_2. The increase in these parameters leads to the dominance of the heat and mass transfer irreversibility over fluid friction irreversibility because of which both profiles increase. It is seen from both profiles that the increase due to the temperature

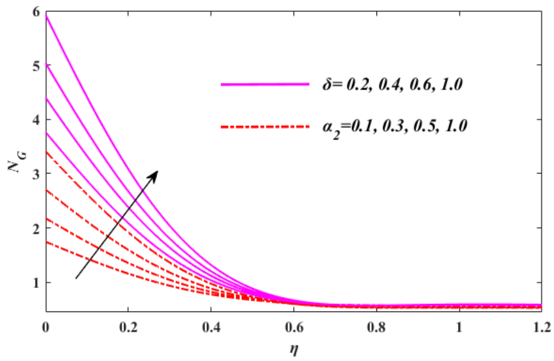

Fig. 11. (Color online) Effects of δ and α_2 upon N_G.

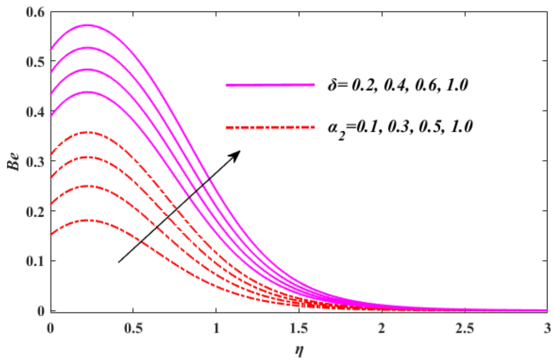

Fig. 12. (Color online) Effects of δ and α_2 upon Be.

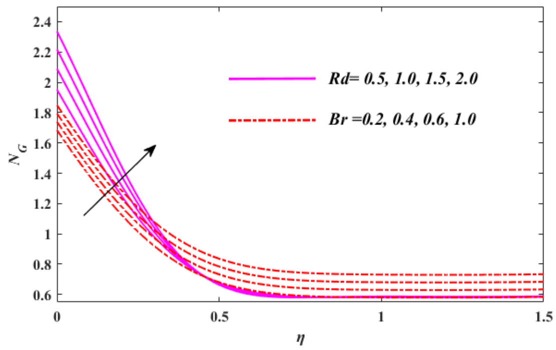

Fig. 13. (Color online) Effects of Rd and Br upon N_G.

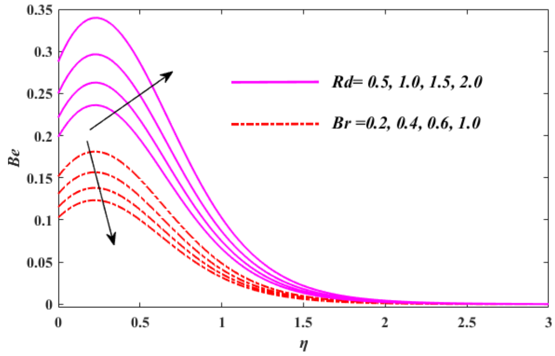

Fig. 14. (Color online) Effects of Rd and Br upon Be.

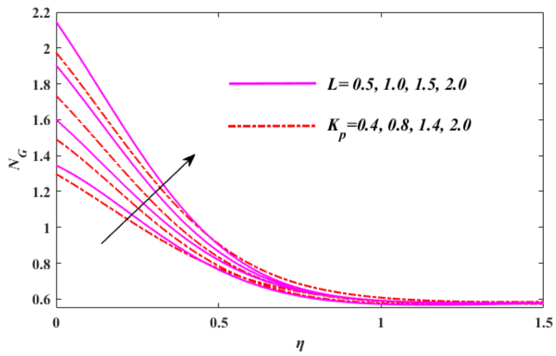

Fig. 15. (Color online) Effects of L and K_p upon N_G.

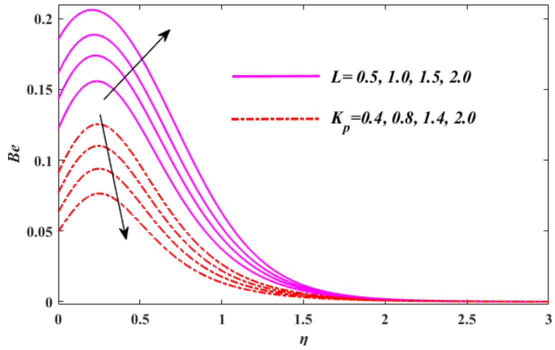

Fig. 16. (Color online) Effects of L and K_p upon Be.

Table 1. Numerical values of local Nusselt number against flow parameters.

λ	γ	Rd	Pr	Ec	N_b	N_t	λ_T	A^*	B^*	$\frac{\mathrm{Nu}_x}{\sqrt{\mathrm{Re}}}$
0.3	0.2	0.5	6.2	0.4	0.1	0.2	0.1	0.1	0.1	0.5229
0.6										0.5335
0.9										0.5440
1.2										0.5545
0.3	0.4									0.5306
	0.8									0.5409
	1.2									0.5509
	0.2	1.0								0.5630
		1.5								0.6055
		2.0								0.7034
		0.5	7.0							0.4245
			8.0							0.3076
			9.0							0.1974
			6.2	0.8						0.4980
				1.4						0.4731
				2.0						0.4233
				0.4	0.3					0.4545
					0.5					0.3907
					0.7					0.3124
					0.1	0.4				0.4431
						0.6				0.3690
						0.8				0.2374
						0.2	0.5			0.4971
							1.0			0.4635
							2.0			0.3911
							0.1	−1.0		0.8572
								0.0		0.5533
								1.0		0.2489
								0.1	−1.0	0.8472
									0.0	0.5536
									0.5	0.3978
									1.0	0.2352

difference parameter δ is more extensive than from the concentration difference parameter α_2.

The influence of the parameters Rd and Br upon N_G and Be is provided in Figs. 13 and 14. The profile of entropy generation N_G increases as Radiation parameter Rd and Brinkman number Br increases. Whereas the profile of Bejan number Be observes two different trends, i.e., rising for Radiation parameter Rd but decreasing for Brinkman number Br. The rise in the radiation parameter leads to the enhancement of the internal energy of the system. Therefore, in this process, the heat and mass transfer irreversibility becomes dominant over fluid friction irreversibility, and as a result, the entropy generation and Bejan number increases. Also, during the enhancement of the Brinkman number Br, a large amount of heat is generated for the fluid particles, due to which disorderedness of the system is increased. As a result, the entropy generation rises, but it decreases the Bejan number Be.

Table 2. Numerical values of local Nusselt number against flow parameters.

λ	γ	Le	Pr	N_b	N_t	λ_C	σ	δ	E	$\frac{\mathrm{Sh}_x}{\sqrt{\mathrm{Re}}}$
0.3	0.2	0.5	6.2	0.1	0.2	0.1	0.5	0.4	1.0	3.1900
0.6										3.1856
0.9										3.1700
1.2										3.1615
0.3	0.4									3.1956
	0.8									3.2005
	1.2									3.2114
	0.2	1.0								3.6446
		1.5								4.0446
		2.0								4.4025
		0.5	7.0							3.3667
			8.0							3.5754
			9.0							3.7711
			6.2	0.3						2.9705
				0.5						2.8118
				0.7						2.5958
				0.1	0.4					3.4055
					0.6					3.6290
					0.8					4.0977
					0.2	0.5				3.1607
						1.0				3.1242
						2.0				3.0516
						0.1	1.0			3.3284
							2.0			3.5862
							3.0			3.8232
							0.3	1.0		3.2287
								1.5		3.2517
								2.0		3.2695
								0.4	2.0	3.1151
									3.0	3.0784
									4.0	3.0605
									5.0	3.0519

Table 3. Comparison table for Nusselt number with Ref. 36 when $N_b = N_t = \mathrm{Ec} = \lambda_T = A^* = B^* = F_r = \alpha = N_r = 0$ and $K_p = \mathrm{Ha}$.

	Newtonian fluid[36]	Newtonian fluid (Present study)	Dilatant fluid[36]	Dilatant fluid (Present study)	Pseudo plastic fluid[36]	Pseudo plastic fluid (Present study)
Rd						
0.5	0.830449	0.830449	0.619279	0.619279	0.888721	0.888721
1	0.776064	0.776064	0.579640	0.579640	0.832591	0.832591
1.5	0.735376	0.735376	0.551215	0.551215	0.790059	0.790059

Figures 15 and 16 deal to predict the effects of the parameters L and K_p upon N_G and Be. The profile of entropy generation N_G is an increasing function of the Diffusion parameter L and the Permeability parameter of the porous medium K_p. On the other hand, the profile of the Bejan number predicts two opposite trends, i.e., escalating for L but decaying for K_p. The rise in the parameter K_p leads to the larger fluid viscosity that produces a resistive force between the fluid particles due to which the disorderedness inside the system escalates, and as a result, entropy generation escalates. It is further noticed that rise in the parameter K_p causes the domination of the fluid friction irreversibility over the heat and mass transfer irreversibility because of which Bejan number decays Be.

7. Physical Quantities

The numerical values of the local Nusselt number and local Sherwood number for different values of the parameters are calculated in Tables 1 and 2. The local Nusselt number increase with R-P fluid parameter λ, Bingham number and thermal relaxation time while a decreasing numerical trend is noted for exponential heat source parameters. The local Sherwood number increases with chemical reaction constant and Lewis number. Table 3 describes comparative result of Nusselt number for different values of radiation parameter. It is seen that our results are very much similar to the previous literature[36] which ensure the validation of our problem.

8. Conclusions

The thermal features of R-P nanomaterial are evaluated in presence of entropy generation, nonuniform heat source, Ohmic dissipation and thermal radiation assessment. The Cattaneo–Christov theories are accounted in the energy and concentration equations to modify the analysis. The non-Darcy porous relations are used to depict the flow through porous space. The shooting technique is used to perform the numerical computations for set of equations which modeled in nonlinear and coupled forms. The summarized observations are as follows:

- R-P fluid parameter enhances the fluid velocity while a decreasing change in velocity in noted with Bingham number and permeability of porous space.

- The progressive nanofluid temperature is noticed for space and temperature-dependent parameters of heat source/sink parameters, Brownian motion and Eckert number.
- A declining change in nanofluid temperature is assessed with thermal relaxation parameter of heat flux.
- The activation energy and thermophoretic constants present an improve nanofluid concentration while decaying results are deduced for concentration relaxation parameter, Prandtl number and Lewis number.
- An increasing variation in Entropy generation and Bejan number is noticed with privilege change in temperature difference parameter, radiation parameter and concentration difference parameter.
- Bejan number declines with permeability parameter and Brinkman number.

References

1. S. U. S. Choi, Enhancing thermal conductivity of fluids with nanoparticles, in *Proc. 1995 ASME Int. Mechanical Engineering Congress and Exposition*, ASME FED 231/MD, Vol. 66, 1995, San Francisco USA, pp. 99–105.
2. E. M. A. Elbashbeshy, T. G. Emam and M. S. Abdel-wahed, *J. Mech. Sci. Technol.* **27**, 3843 (2013).
3. N. Bachok, A. Ishak and I. Pop, *ASME J. Heat Transf.* **135**, 1 (2013).
4. P. K. Kameswaran *et al.*, *Int. J. Heat Mass Transf.* **55**, 7587 (2012).
5. M. Narayana and P. Sibanda, *Int. J. Heat Mass Transf.* **55**, 7552 (2012).
6. H. U. Kang, S. H. Kim and J. M. Oh, *Exp. Heat Transf.* **19**, 181 (2006).
7. V. Y. Rudyak, A. A. Belkin and E. A. Tomilina, *Tech. Phys. Lett.* **36**, 660 (2010).
8. E. M. A. Elbashbeshy, T. G. Emam and M. S. Abdel-Wahedan, *Heat Mass Transf.* **50**, 57 (2014).
9. K. Jafar *et al.*, *Can. J. Chem. Eng.* **90**, 1336 (2012).
10. K. B. Pavlov, *Magn. Gidrodin.* **4**, 146 (1974).
11. C. Cattaneo, *Atti Semin. Mat. Fis. Univ. Modena Reggio Emilia* **3**, 83 (1948).
12. C. I. Christov, *Mech. Res. Commun.* **36**, 481 (2009).
13. B. Straughan, *Int. J. Heat Mass Transf.* **53**, 95 (2010).
14. S. Han *et al.*, *J. Pre-proof Appl. Math. Lett.* **38**, 87 (2014).
15. T. Hayat *et al.*, *Result Phys.* **9**, 290 (2018).
16. T. Hayat *et al.*, *Chin. J. Phys.* **55**, 916 (2017).
17. J. Li, L. Zheng and L. Liu, *J. Mol. Liq.* **221**, 19 (2016).
18. J. Sui, L. Zheng and X. Zhang, *Int. J. Thermal Sci.* **104**, 461 (2016).
19. M. G. Reddy *et al.*, *J. Braz. Soc. Mech. Sci. Eng.* **40**, 95 (2018).
20. K. G. Kumar, *Int. J. Numer. Methods Heat Fluid Flow* **30**, 1991 (2019).
21. K. G. Kumar, *Int. J. Numer. Methods Heat Fluid Flow* **30**, 2051 (2019).
22. A. Rauf *et al.*, *Appl. Math. Mech.* **39**, 467 (2018).
23. J. N. Kapur and R. C. Gupta, *Appl. Sci. Res., Sec. A* **14**, 13 (1965).
24. S. Ghoshal, *Chem. Eng. Sci.* **26**, 185 (1971).
25. T. Y. Na, *Int. J. Non-Linear Mech.* **29**, 871 (1994).
26. K. S. Yam *et al.*, *Int. J. Non-Linear Mech.* **44**, 1056 (2009).
27. M. M. Khader and A. M. Megahed, *Eur. Phys. J. Plus* **129**, 10 (2014).
28. M. I. Khan and F. Alzahrani, *Int. J. Hydrog. Energy* **46**, 1362 (2021).
29. M. M. Khader and A. M. Megahed, *J. Heat Transf.* **136**, 072602 (2014).

30. M. I. Khan *et al.*, *Surf. Interfaces* **22**, 100849 (2021).
31. M. M. Khader and A. M. Megahed, *Transp. Porous Media* **105**, 487 (2014).
32. M. Nazeer *et al.*, *Surf. Interfaces* **22**, 100846 (2021).
33. A. M. Megahed, *J. Mech.* **30**, 395 (2014).
34. M. I. Khan *et al.*, *J. Colloid Interface Sci.* **498**, 85 (2017).
35. A. M. Megahed, *Meccanica* **50**, 1693 (2015).
36. M. G. Reddy and S. Rani, *Mod. Phys. Lett. B* 1950449 (2019).